NEUROSCIENCE

Molecular and functional architecture of the mouse photoreceptor network

Nange Jin[1], Zhijing Zhang[1], Joyce Keung[1], Sean B. Youn[2,3], Munenori Ishibashi[1], Lian-Ming Tian[1], David W. Marshak[4,5,6,7], Eduardo Solessio[8], Yumiko Umino[8], Iris Fahrenfort[1], Takae Kiyama[1], Chai-An Mao[1,5,6,7], Yanan You[9,10], Haichao Wei[9,10], Jiaqian Wu[6,7,9,10], Friso Postma[11]*, David L. Paul[11], Stephen C. Massey[1,2,5,6,7,12†], Christophe P. Ribelayga[1,2,5,6,7,13,14†]

Mouse photoreceptors are electrically coupled via gap junctions, but the relative importance of rod/rod, cone/cone, or rod/cone coupling is unknown. Furthermore, while connexin36 (Cx36) is expressed by cones, the identity of the rod connexin has been controversial. We report that FACS-sorted rods and cones both express *Cx36* but no other connexins. We created rod- and cone-specific *Cx36* knockout mice to dissect the photoreceptor network. In the wild type, Cx36 plaques at rod/cone contacts accounted for more than 95% of photoreceptor labeling and paired recordings showed the transjunctional conductance between rods and cones was ~300 pS. When *Cx36* was eliminated on one side of the gap junction, in either conditional knockout, Cx36 labeling and rod/cone coupling were almost abolished. We could not detect direct rod/rod coupling, and cone/cone coupling was minor. Rod/cone coupling is so prevalent that indirect rod/cone/rod coupling via the network may account for previous reports of rod coupling.

INTRODUCTION

Light absorption and phototransduction by rods and cones represent the initial steps of vision (*1*). In addition, photoreceptor signals can spread laterally to neighboring photoreceptors via gap junctions. Gap junctions are made of connexins and form intercellular channels that allow electrical coupling between adjacent cells (*2*, *3*). Furthermore, gap junctions are common circuit elements used for signal averaging, noise reduction, and network synchronization in many brain regions (*2*, *3*).

In the mammalian retina, ultrastructural evidence has identified a variety of gap junctions at photoreceptor terminals. Early electron microscopy (EM) studies in various species, including primate, suggested that gap junctions may be present at contacts between cone pedicles (*4*–*8*), between rod spherules (*8*), and between rod spherules and cone pedicles (*4*, *6*, *8*, *9*). However, histochemical studies on the identity of the connexin expressed in photoreceptors have yielded more equivocal evidence. Although it is well established that cones express connexin36 (Cx36) (*10*, *11*), the identity of the rod connexin remains unsettled, centering on whether rods express Cx36 or not (*10*–*14* [reviewed in (*15*, *16*)]. In summary, the complexity of the network, with the potential for indirect coupling, and the unknown rod connexin represent major roadblocks that have hindered our understanding of the mechanistic basis of photoreceptor coupling and its role in retinal function.

Physiological studies have suggested several functional advantages for photoreceptor coupling. For example, coupling between cones may improve discrimination of signal from noise (*17*). Coupling between rods may reduce rod response variability due to signal averaging within the coupled network (*18*–*20*). Rod/cone coupling may provide a route for rods signals to enter cones (*18*, *21*–*26*) and cone-connected horizontal cells (*27*, *28*). Yet, the function of photoreceptor coupling remains puzzling. For instance, under dim light, when vision relies on single photons, rod coupling is expected to decrease the amplitude of single-photon responses and thereby the transmission of single-photon events through the primary rod pathway, with obvious detrimental consequences on vision (*9*, *29*). In addition, while rod/cone coupling is necessary to allow rod signals to enter the secondary rod pathway, the contribution of this pathway is unclear (*30*).

To isolate the contributions of rod/rod, cone/cone, and rod/cone coupling and directly test whether Cx36 is the rod connexin, we made rod- and cone-specific *Cx36* conditional knockout (XO) mice. In each of our mutant lines, we examined the distribution and expression of Cx36 and measured the transjunctional conductance between pairs of adjacent photoreceptors (*31*, *32*). We also recorded the light responses of cones. Our results show that Cx36 is necessary and sufficient for photoreceptor coupling and that rod/cone coupling is predominant in the photoreceptor network. We could not detect direct rod/rod coupling and propose that indirect rod/cone/rod

[1]Ruiz Department of Ophthalmology and Visual Science, McGovern Medical School, UTHEALTH-The University of Texas Health Science Center at Houston, Houston, TX, USA. [2]Summer Research Program, McGovern Medical School, UTHEALTH-The University of Texas Health Science Center at Houston, Houston, TX, USA. [3]Undergraduate Program, William Marsh Rice University, Houston, TX, USA. [4]Department of Neurobiology and Anatomy, McGovern Medical School, UTHEALTH-The University of Texas Health Science Center at Houston, Houston, TX, USA. [5]Neuroscience Research Center, UTHEALTH-The University of Texas Health Science Center at Houston, Houston, TX, USA. [6]Graduate School of Biomedical Sciences, MD Anderson Cancer Center/UTHEALTH-The University of Texas Health Science Center at Houston, Houston, TX, USA. [7]Program in Neuroscience, Graduate School of Biomedical Sciences, MD Anderson Cancer Center/UTHEALTH-The University of Texas Health Science Center at Houston, Houston, TX, USA. [8]Center for Vision Research and SUNY Eye Institute, Department of Ophthalmology, SUNY Upstate Medical University, Syracuse, NY, USA. [9]The Vivian L. Smith Department of Neurosurgery, McGovern Medical School, The University of Texas Health Science Center at Houston, Houston, TX, USA. [10]Center for Stem Cell and Regenerative Medicine, The University of Texas Brown Foundation Institute of Molecular Medicine, Houston, TX, USA. [11]Department of Neurobiology, Medical School, Harvard University, Boston, MA, USA. [12]Elizabeth Morford Distinguished Chair in Ophthalmology and Research Director, Ruiz Department of Ophthalmology and Visual Science, McGovern Medical School, UTHEALTH-The University of Texas Health Science Center at Houston, Houston, TX, USA. [13]Program in Biochemistry and Cellular Biology, Graduate School of Biomedical Sciences, MD Anderson Cancer Center/UTHEALTH-The University of Texas Health Science Center at Houston, Houston, TX, USA. [14]Bernice Weingarten Chair in Ophthalmology, Ruiz Department of Ophthalmology and Visual Science, McGovern Medical School, UTHEALTH-The University of Texas Health Science Center at Houston, Houston, TX, USA.
*Present address: Cohen Veterans Bioscience, New York Office 535 8th Ave, 12th floor, New York, NY 10018, USA.
†Corresponding author. Email: christophe.p.ribelayga@uth.tmc.edu (C.P.R.); steve.massey@uth.tmc.edu (S.C.M.)

coupling accounts for previous reports of rod coupling. Rod/cone coupling provides an entry to the secondary rod pathway, which supplies rod inputs to retinal ganglion cells at intermediate intensities (*1*, *30*). We conclude that rod/cone gap junctions are the keystone of the mouse photoreceptor network and are well placed to influence many retinal circuits.

RESULTS

Cx36 expression in mouse photoreceptors

The mammalian retina is a well-organized laminar structure with three cellular layers separated by two synaptic or plexiform layers (fig. S1) (*1*). The outer nuclear layer (ONL) contains the cell bodies of both rods and cones. The relative abundance of rods and cones varies across mammalian species. For example, the ground squirrel retina is cone dominated (*33*), and in primates, the rod/cone ratio depends on eccentricity, from the cone-dominated fovea to the rod-dominated periphery (*34*). In the mouse retina, rods far outnumber cones by 30:1, filling most of the layers in the ONL, while cones account for only 3% of photoreceptors (*1*, *35*). Cones are found in the top or most distal layers of the ONL, descending via long axons to a row of prominent terminals or pedicles, ~10 μm in diameter, in the middle of the outer plexiform layer (OPL). Below each cone pedicle, the dendrites of many bipolar cells and horizontal cells converge while rod spherules fill the space between and above the cone pedicles. Rod spherules are 2 to 3 μm in diameter and contain a postsynaptic compartment, which processes enter via a narrow mouth or synaptic invagination (*1*). Thus, in the OPL, cone pedicles and rod spherules are readily identified by size, location, and structure.

Labeling for the gap junction protein Cx36 shows that the OPL contains many small immunoreactive puncta, approaching the limit of confocal resolution (Fig. 1A and fig. S1). They are much smaller than those of the AII amacrine cells, which dominate the inner plexiform layer (IPL). The Cx36-positive puncta or plaques likely represent gap junctions. They may be divided into two groups depending on their location and colocalization with cone pedicles. First, Cx36 plaques are colocalized with cone pedicles on telodendria, which extend laterally and upward (Fig. 1, B and C). The Cx36 plaques associated with the cone pedicles show as white in the colocalization analysis. Furthermore, the cone pedicle Cx36 labeling is all contained within the band of rod spherules, which fill the upper part of the OPL. There is no Cx36 labeling in the ONL. Second, distinctly below and separate from each cone pedicle, there is a cluster of Cx36 puncta (circled in Fig. 1C). These plaques represent gap junctions that are not associated with cones but instead are located on bipolar cell dendrites where they converge beneath the cone pedicle (*4*, *10*, *13*). Because they are separate from the cones, they remain red in the colocalization analysis (Fig. 1C) and are excluded from further analysis.

In whole-mount retina, Cx36 is clearly associated with the matrix of cone telodendria, which form an overlapping substrate for photoreceptor coupling (Fig. 1B and fig. S2). In retinal sections, Cx36 labeling is found at sites where cone telodendria contact the base of each rod spherule (Fig. 1, C and D). We estimated that each and every rod (116 of 116) was typically connected to a cone pedicle from 1 to 6 [mean = 2.4 + 1.0 (SD), n = 116] Cx36-positive puncta (Fig. 1D and fig. S2). These observations, which are consistent with previous EM studies (*4*, *6*, *8*, *9*), suggest that, although cones represent ~3% of mouse photoreceptors (*35*), every rod may have direct electrical access to a cone and that each cone may receive electrical signals from ~30 surrounding rods. In summary, the imaging data suggest that rod/cone coupling is ubiquitous and that all rods are coupled to cones by Cx36 gap junctions.

Rod- and cone-specific *Cx36* XO lines

To directly test whether Cx36 is the rod connexin and simplify the analysis of the OPL, we constructed both rod- and cone-specific *Cx36* XO mice for comparison with both wild-type and pan-*Cx36* knockouts (KOs). Gap junctions require a contribution from both coupled cells. Each adjacent cell must contribute a hemichannel, a pair of which can dock to form a gap junction. If one side of a potential pair does not express the appropriate connexin, then there can be no gap junction. Eliminating either hemichannel is sufficient to prevent the formation of a gap junction (*36*). Therefore, in the cone-*Cx36* XO, we would expect to eliminate rod/cone coupling and cone/cone coupling leaving rod/rod coupling unchanged. Conversely, in the rod-*Cx36* XO, both rod/cone coupling and rod/rod coupling should be abolished while unmasking cone/cone coupling. Obviously, in the pan-*Cx36* KO, all Cx36 plaques should be gone. Thus, these *Cx36* mutants provide a set of powerful tools to analyze the contributions of rods and cones to photoreceptor coupling (see fig. S3 for a schematic representation).

Cx36 expression in the OPL was greatly reduced in both rod-*Cx36* XO and cone-*Cx36* XO retinas (Fig. 2A and fig. S4). On the basis of the mean area (Fig. 2B) or the mean intensity of the fluorescence signal (fig. S5), we estimated that the reduction in Cx36 labeling was >95% in the OPL in both conditional XO lines compared to their respective wild-type littermates (ctl) or C57BL/6J (B6) mice. In contrast, the normal dense pattern of Cx36 expression in the IPL was still observed, indicating that the conditional knockout lines are specific to photoreceptors (figs. S4 and S5). Despite the massive reduction of Cx36 labeling in the OPL, it should be noted that the Cx36 associated with bipolar cells, underneath each cone pedicle, remained. This persistence (Fig. 2A, white circles) suggests that the reduction in Cx36 signal in the OPL in the mutant lines resulted primarily from the elimination of photoreceptor gap junctions. Last, as expected, in the pan-*Cx36* KO mice, there was a near-total absence of signal throughout the retina (Fig. 2A and figs. S4 and S5).

In summary, the rod-*Cx36* XO and the cone-*Cx36* XO had almost the same effect; both caused a massive reduction in Cx36 labeling in the OPL, as if they affected different parts of the same target. Because blocking connexin expression on either side will prevent the formation of rod/cone gap junctions, this result suggests that (i) most of the missing plaques are rod/cone gap junctions mediated by Cx36, and (ii) because rod/cone plaques are eliminated in the rod-*Cx36* XO, then rods must express Cx36.

Quantitative analysis of Cx36 labeling

We made a quantitative analysis of Cx36-positive plaque numbers and volume in the OPL, normalized to the number of cone pedicles, from whole-mount preparations. Excluding the plaques beneath each cone associated with bipolar cell dendrites, we estimated that a z stack made of 7 to 15 45 μm by 45 μm by 0.4 μm (x, y, z) sections that included the OPL contained, on average, ~45 Cx36 plaques per cone pedicle in wild-type retinas. In the cone-*Cx36* XO, which should reveal rod/rod gap junctions, there were ~0 Cx36 immunoreactive puncta, not significantly different from the pan-*Cx36* KO (Fig. 2C and fig. S6). Thus, in the cone-*Cx36* XO, which should delete cone/cone and

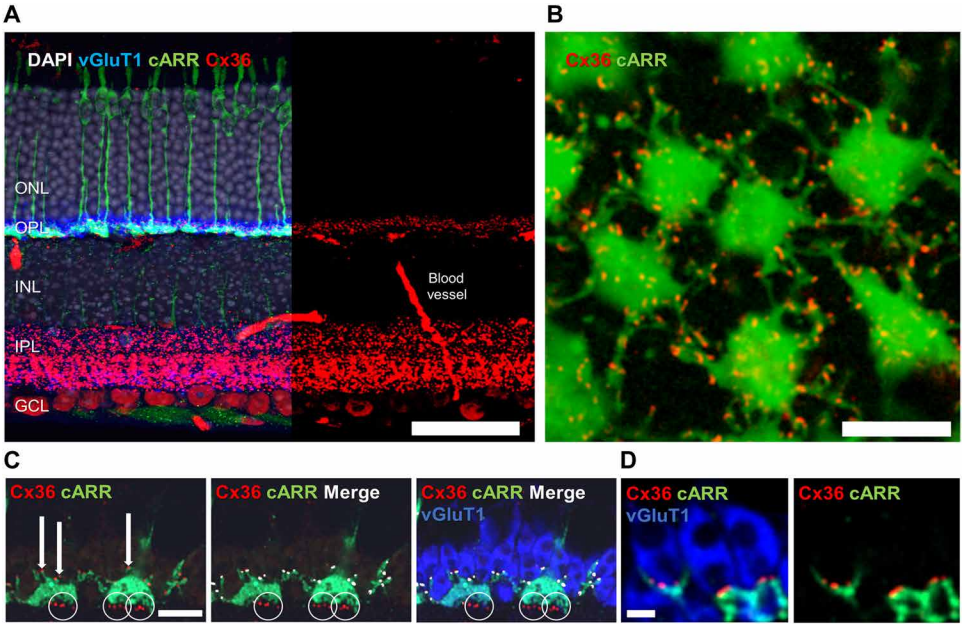

Fig. 1. Cx36 at rod/cone contacts. (**A**) Four-channel labeling of wild-type mouse (B6) retinal section. Cones labeled for cone arrestin (cARR green), rod spherules for the vesicular glutamate transporter 1 (vGluT1, blue), and nuclei stained with 4′,6-diamidino-2-phenylindole (DAPI) (gray). For clarity, only Cx36 (red) in right half. Cx36 labeling is very dense in the IPL, less so in the OPL. Note that cone pedicles, rod spherules, and Cx36 contained in the OPL. Scale bar, 50 μm. (**B**) In whole-mount retina, OPL shows Cx36 plaques (red) associated with cone telodendria (green). Scale bar, 10 μm. (**C**) High magnification (Zeiss LSM800 Airyscan), wild-type mouse retina showing Cx36 plaques (red) associated with cone telodendria (green, arrows) and distinctly beneath the cone pedicles (circled). Colocalization (white) highlights Cx36 on telodendria, not underneath cone pedicles (circled). Colocalized Cx36/cone pedicle sites are contained within the band of rod spherules (vGlut1, blue). Scale bar, 10 μm, applies to all. (**D**) Left; Representative example shows three rod spherules (blue) and cone telodendria (green) with multiple Cx36 puncta (1 to 4, red) at each contact. Right: No blue channel for clarity. Scale bar, 1 μm, applies to both.

rod/cone gap junctions, we were unable to detect rod/rod Cx36-positive puncta. In rod-*Cx36* XO retinas, there were ~2 to 4 Cx36 plaques per cone pedicle, yet this was significantly different from either the cone-*Cx36* XO or pan-*Cx36* KO. Since the rod-*Cx36* XO should delete rod/cone and rod/rod gap junctions to expose cone/cone coupling, this may indicate the presence of a few cone/cone Cx36 gap junctions. The few Cx36-positive plaques that we found in the rod-*Cx36* XO were located on the cone telodendria, possibly at cone-to-cone contacts (fig. S7). The absence of Cx36 signal at points of contact between rods and cones in the rod-*Cx36* XO strengthens the view that rods express Cx36. Last, assuming a rod/cone ratio of 30:1 (*35*), we can estimate that in the wild type, there are approximately 1.5 (or 45:30) plaques per rod spherule, indicating that many rods make more than one gap junction with cones. Together, our observations suggest that rod/cone gap junctions dominate the OPL and that rods express Cx36 at rod/cone gap junctions. The absence of Cx36 labeling in the cone-*Cx36* XO, which should unmask rod/rod gap junctions, questions the very existence of direct electrical coupling between rods.

Analyzing the volume of the Cx36 plaques revealed a major difference in size between and within genotypes. In the wild type, plaque volume ranged from 0.008 to 1.943 μm^3 with a median of 0.062 μm^3 (Fig. 2D and fig. S6C). We estimated the limit of detection of the confocal microscope at ~0.2 μm by 0.2 μm by 0.5 μm (*x*, *y*, *z*) or 0.02 μm^3. Plaque volumes in the pan-*Cx36* KO and the cone-*Cx36* XO lines were close to noise with medians smaller or equal to 0.020 μm^3 (Fig. 2D and fig. S6C). Plaque volume in the rod-*Cx36* XO was slightly higher (median = 0.022 μm^3), indicating that cone/cone Cx36-positive puncta are hardly distinguishable from the noise. Thus, rod/cone plaques, which likely represent the largest fraction of the gap junctions in the wild-type OPL, are bigger and display a high degree of heterogeneity in size. Likewise, the cone/cone gap junctions, which likely represent a large fraction of the particles present in the rod-*Cx36* XO OPL, exhibit some heterogeneity in size as well, but their average volume is close to the limit of detection of the confocal microscope, suggesting that the cone/cone gap junctions are smaller than the rod/cone gap junctions on average. Heterogeneity in photoreceptor coupling is consistent with measures of plaque size [fig. S6C; see also (*10*, *11*, *37*, *38*)], measures of the fraction of phosphorylated Cx36 plaques in the OPL (*11*, *38*), and measures of the junctional conductance [(*31*); also see below].

Genetic and EM data on Cx36

We tested three important facets of our model. First, we evaluated the expression profile of connexins in rods and cones using our CRE-reporter lines and fluorescence-assisted cell sorting (FACS). RNA sequencing (RNA-seq) and analysis showed that both cones and rods express *Cx36* mRNA. Furthermore, no other known connexins were expressed in either rods or cones (fig. S8A). This eliminates the possibility that another connexin could be up-regulated in the absence of Cx36 or that rod/cone gap junctions could be heterotypic and/or heteromeric, that is constructed from two different connexins. Second, because knocking out *Cx36* in one photoreceptor cell type could perhaps reduce the expression of *Cx36* in the other, we probed *Cx36* transcript expression in our mutant lines using fluorescence in situ hybridization (FISH-RNAscope). We found that eliminating *Cx36* expression in one photoreceptor type does not significantly alter its expression in the other type (fig. S8B). Last, we

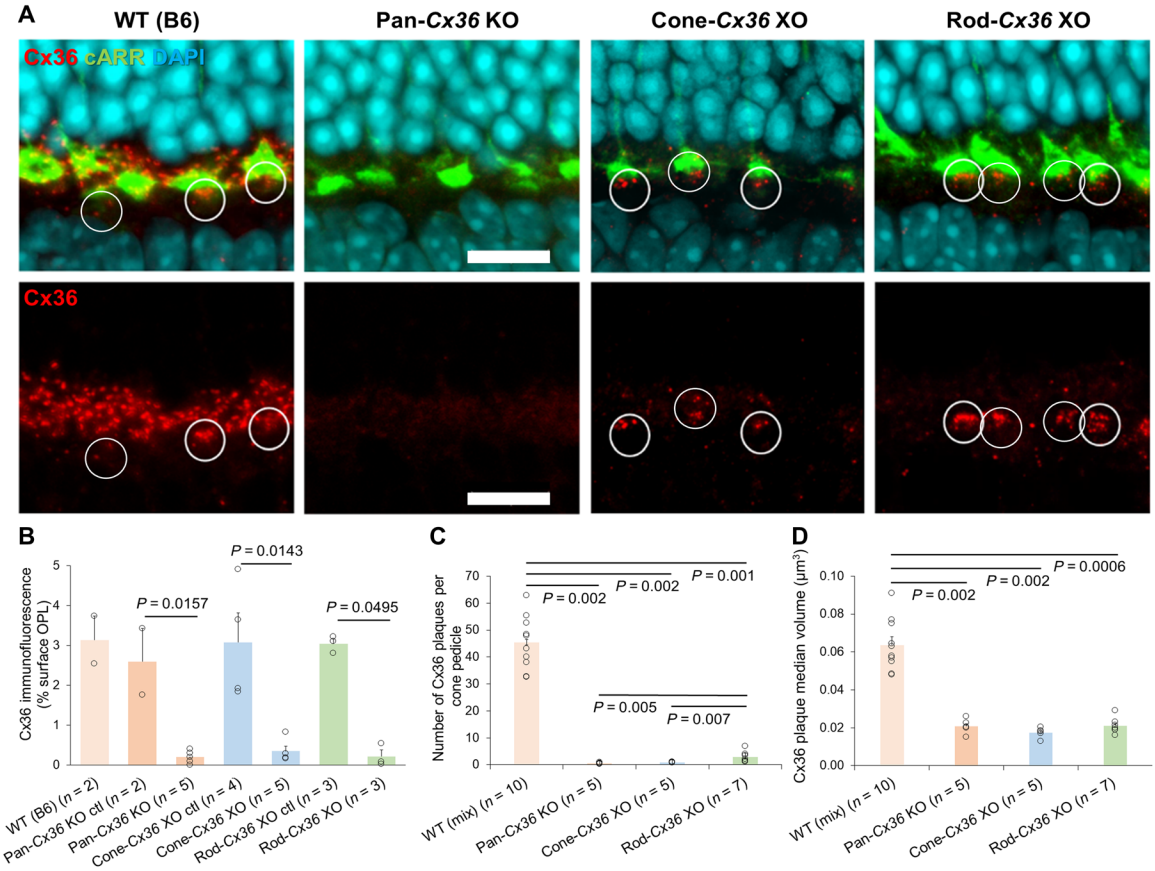

Fig. 2. Cx36 distribution in pan- and conditional-*Cx36* knockouts. (**A**) OPL of wild type (WT; B6), and *Cx36* mutants labeled for Cx36 (red) and cone arrestin (green). Top row: cell nuclei stained with DAPI (cyan). Bottom row: Cx36 only for clarity. Note the absence of Cx36 in the pan-*Cx36* KO and large reduction in cone- or rod-*Cx36* XO. Cx36 beneath cone pedicles (white circles) associated with bipolar cell dendrites, not cones. Scale bars, 10 μm, applies to all. (**B**) Quantification of Cx36 in the OPL for wild type and *Cx36* mutants; individual values (black circles), means (bars), SEM (error bars), and *n* = number of animals. Statistical test between mutants and respective control littermates (ctl), nonparametric Kruskal-Wallis analysis of variance (ANOVA). (**C**) Cx36 plaques in the OPL per cone pedicle for wild type and *Cx36* mutants. Analysis performed on 7 to 15 sections (45 μm by 45 μm by 0.4 μm) spanning the OPL. Cx36 underneath cone pedicles excluded from the analysis. Wild-type column included B6 mice and mutant littermates (mix). Presentation as in (B). Only statistically significant differences shown ($P < 0.05$), nonparametric Kruskal-Wallis ANOVA. (**D**) Averaged median volume of the Cx36 puncta identified in (C), presentation as in (B).

used immuno-EM to locate gap junctions in the wild-type retina. Cx36 labeling sign posts gap junctions found at contacts between rods and cones. In addition, Cx36 was clearly present on both sides of rod/cone gap junctions, suggesting that both rods and cones express Cx36 (fig. S8C). However, we were unable to identify rod/rod or cone/cone gap junctions.

Together, the data indicate that (i) both rods and cones express Cx36, and there is no evidence for the presence of another connexin in photoreceptors. Thus, rod/cone coupling is served by homotypic Cx36/Cx36 gap junctions; (ii) more than 95% of the Cx36 plaques occur at rod/cone contacts; (iii) Cx36 plaques between cones are rare; and (iv) the lack of visible Cx36-positive puncta between rod spherules questions the existence of direct rod/rod coupling. Thus, gap junction formation between photoreceptors requires Cx36, and rod/cone gap junctions are predominant in the photoreceptor network.

Cx36 requirement and routes of electrical coupling between photoreceptors

Paired recordings

We made paired recordings to test directly whether Cx36 is required for electrical coupling between photoreceptors (Fig. 3, A to C). First, we measured the transjunctional conductance between rod pairs, between cone pairs, and between rod/cone pairs in pan-*Cx36* KO mice and littermate controls. We set the threshold for coupling at 50 pS to exceed the baseline noise. In the control retinas, rod/rod (19 coupled pairs of 21 recorded pairs) and cone/cone coupling (10 of 11 pairs) were modest, ~100 pS, but rod/cone coupling (15 of 15 pairs) was much larger, ~300 pS (see Table 1 for details). In the pan-*Cx36* KO mice, we found that the rod/rod (2 of 8 pairs), rod/cone (0 of 6 pairs), and cone/cone (7 of 13 pairs) junctional conductances were all close to or below the resolvable limit given the measurement noise (Fig. 3, D to F, and Table 1). These results strongly implicate Cx36 in electrical coupling between photoreceptors and confirm that no compensation or up-regulation of another connexin plays a role in the process in the absence of Cx36. However, if rod/rod coupling is indirect via an intermediary cone, i.e., rod/cone/rod, then eliminating the cone expression of Cx36 would block indirect rod coupling regardless of the identity of the rod connexin. Thus, this result may not identify the rod connexin, and it leaves open the theoretical possibility that rods express another connexin.

Therefore, we made conductance measurements between photoreceptor pairs in both the rod- and cone-specific *Cx36* XOs (Fig. 3, G to I;

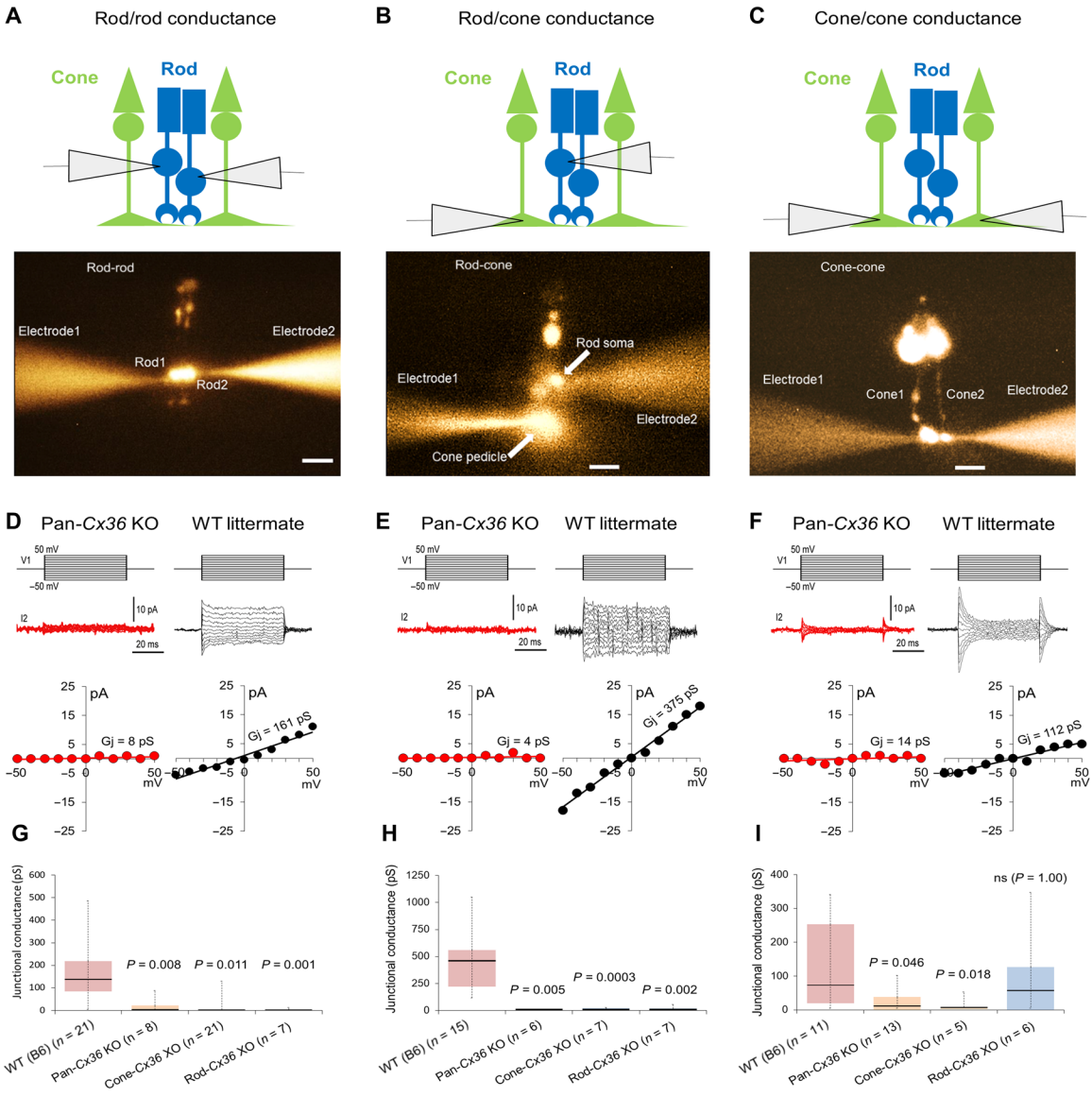

Fig. 3. Cx36 requirement and routes of electrical coupling between photoreceptors. (**A** to **C**) Schematic representation of the experimental setup and visualization of the photoreceptors simultaneously patch-clamped and filled with Lucifer yellow through the two recoding pipettes. Simultaneous patch clamp recording of photoreceptor pairs in the living mouse retinal slice are illustrated for a pair of rods (A), a rod/cone pair (B), and a cone/cone pair (C). (**D** to **F**) Examples of simultaneous voltage clamp recordings from rod/rod (D), cone/cone (E), and rod/cone (F) pairs obtained in pan-*Cx36* KO retinas (red traces) and their respective wild-type control littermates (black traces). Transjunctional current traces in response to 50-ms voltage steps, 10-mV increments from −50 to +50 mV, and the voltage-current relationship whose slope gives an estimate of the transjunctional conductance are shown. (**G** to **I**) Rod/rod (G), rod/cone (H), and cone/cone (I) coupling conductances in wild-type (B6) and *Cx36* mutant mice. Box plots show the median value (center line), the lower (25%) and upper (75%) quartiles, and minimum and maximum (whiskers). Statistical test: nonparametric Kruskal-Wallis ANOVA. ns, not significant.

see Table 1 and figs. S9 and S10 for details). Rod/rod coupling was abolished in the rod-specific *Cx36* XO (1 or 7 pairs). This indicates that rods express Cx36. Likewise, cone/cone coupling was eliminated in the cone-specific *Cx36* XO (3 of 7 pairs), as expected. In addition, rod/cone coupling was almost abolished both in rod-*Cx36* XO (2 of 7 pairs) and cone-*Cx36* XO mutants (2 of 7 pairs), indicating that Cx36 is required on both sides of the rod/cone gap junction for functional coupling (Fig. 3H). In the absence of evidence to support the presence of another connexin in photoreceptors (fig. S8A), these data establish that Cx36 is necessary and sufficient for electrical coupling between photoreceptors.

Rod coupling is indirect

The rod- and cone-specific *Cx36* XOs also helped to determine whether coupling between rods is direct (rod/rod) or indirect (rod/cone/rod). In cone-*Cx36* XO retinas, where cone/cone and rod/cone gap junctions have been eliminated and only direct rod/rod coupling is expected to persist, we found that electrical coupling between rods (6 of 21 pairs) was reduced by >95% (Fig. 3G and Table 1). The requirement for cone Cx36 indicates that rods are coupled indirectly via an intermediary cone, i.e., rod/cone/rod coupling. Furthermore, the absence of direct rod coupling is consistent with the lack of Cx36 immunoreactivity observed between rod spherules (Fig. 1 and fig. S2).

Table 1. Summary of the junctional conductance measurements. Data shown are the number of pairs recorded *n* (number of uncoupled pairs/number of coupled pairs) and the median value [interquartile] of rod/rod, rod/cone, and cone/cone transjunctional conductances measured in wild type [WT (B6)], pan or conditional knockouts, and their respective control littermates. A pair was considered coupled when conductance is >50 pS. Statistical differences between the mutant lines and their respective control groups are indicated (*$P < 0.05$), nonparametric Kruskal-Wallis ANOVA. The median values of the four WT/control groups were averaged, and the mean (SEM) is shown in the bottom row. See figs. S9 and S10 for more details.

	n	Rod/rod coupling (pS)	*n*	Rod/cone coupling (pS)	*n*	Cone/cone coupling (pS)
WT (B6)	21(2/19)	135 [85,219]	15(0/15)	453 [219,560]	11(1/10)	72 [26,234]
Rod-*Cx36* XO	7(6/1)	0 [0,0]*	7(5/2)	0 [0,1]*	6(2/4)	56 [9,114]
Rod-*Cx36* ctl	7(0/7)	139 [102,254]	11(1/10)	213 [128,574]	7(3/4)	65 [0,126]
Cone-*Cx36* XO	21(15/6)	0 [0,3]*	7(5/2)	0 [0,4]*	5(2/3)	3 [0,5]*
Cone-*Cx36* ctl	7(2/5)	108 [52,111]	12(0/12)	313 [156,654]	20(4/16)	46 [5,224]
Pan-*Cx36* KO	8(6/2)	0 [0,21]*	6(6/0)	0 [0,0]*	13(6/7)	10 [0,38]*
Pan-*Cx36* ctl	14(2/12)	129 [46,161]	7(1/6)	249 [104,306]	20(3/17)	53 [32,129]
Mean WT/ctl	4	128 (7)	4	307 (53)	4	59 (6)

Because our previous work suggested that rod electrical coupling can be pharmacologically increased by blocking dopamine D_2-like receptor activity (*20*), we measured rod coupling strength in cone-*Cx36* XO retinas in the presence of the D_2-like receptor antagonist spiperone (Fig. 4A). Of the four pairs of adjacent rods we recorded, none showed significant conductance (0 of 4 pairs), indicating that in the absence of rod/cone gap junctions, rod/rod coupling is insensitive to spiperone. In contrast, the coupling between wild-type rod/cone pairs was markedly enhanced by spiperone (11 of 11 pairs) (Fig. 4B), which would in turn increase indirect rod/cone/rod coupling. Similarly, the coupling between wild-type rod/cone pairs was markedly decreased by quinpirole (2 of 5 pairs) (Fig. 4B), which would in turn decrease indirect rod/cone/rod coupling. Thus, the data indicate that the primary route of electrical coupling between rods is indirect through an intervening cone. The predominance of the rod/cone gap junction in the network (Fig. 1) and the observation that almost any pair of adjacent rods is electrically coupled in the presence of spiperone in the wild-type retina, that is, in the presence of functional rod/cone gap junctions (*20*, *31*), further support this view.

A similar analysis of the data presented in Fig. 3 helped to define the routes of coupling between cones as well. A comparison of the junctional conductance between directly adjacent cone pedicles in rod-*Cx36* XO mice with their wild-type littermates (Fig. 3I) shows that cone/cone coupling was not significantly different in the absence of Cx36 in the rods (4 of 6 pairs). These measures are also close to estimates of the cone/cone conductance obtained in wild-type (B6) retinas (Fig. 3I, Table 1, and fig. S10). The results suggest that intervening rods contribute little to electrical coupling between cones; therefore, electrical coupling between cones is essentially direct.

In summary, paired recordings show that both rods and cones express Cx36 and that Cx36 is necessary and sufficient for photoreceptor coupling. Rod/cone gap junctions require Cx36 on both sides and exhibit the largest conductance (~300 pS versus ~50 pS for cone/cone gap junctions and ~0 pS for rod/rod gap junctions). Rod/cone coupling also provides a route for indirect coupling between rods (i.e., rod/cone/rod). Although cone/cone coupling is small, it appears to be direct (i.e., cone/cone) because it is still present in the rod-*Cx36* XO. We conclude that rod/cone coupling dominates the photoreceptor network in both size and number.

Functional importance of the rod/cone pathway

The large conductance we measured at rod/cone gap junctions combined with the prevalence of rod/cone gap junctions (Fig. 3H, Table 1, and fig. S10) suggests that these electrical synapses might represent an important functional pathway in the retina. We reasoned that if the rod/cone gap junction is indeed the entry of an important rod pathway, then signals that originate in rods should be observed in cone pedicles in wild-type animals and absent in rod- or cone-*Cx36* KO animals.

Rod input to cones

Light-evoked signals that originate in rods are known to enter cones through rod/cone gap junctions and alter the cone membrane potential in a way that directly reflects the low threshold and slow kinetics of the rod light responses (*21*, *22*). Two recent studies, using the pan-*Cx36* KO line, have implicated Cx36 in the transmission of rod signals to cones (*25*, *26*). However, these results may be expected if cones express Cx36, and therefore, they do not directly address the identity of the rod connexin.

To determine whether the transfer of rod signals to cones requires Cx36 on both sides of the rod/cone gap junction, we recorded cone light responses in the rod- and cone-specific *Cx36* XO mice. We found that wild-type cone voltage responses have an apparent threshold (established as the intensity to elicit a 1-mV response from intensity-response curves) around 0.4 effective isomerization (*R**)/rod/20-ms flash, slightly above rod threshold (~0.2 *R**/rod/20-ms flash), and slow kinetics characterized by the presence of rod after potentials (Fig. 5, A to C). The low threshold of the cone response reflects the important convergence of rods onto cones (~30:1; Figs. 1C and 2C) and the ability of rods to detect and transmit single photons (*20*, *29*). Under these conditions, the cone membrane potential is able to sense a few single-photon responses that occur simultaneously within the pool of rods coupled to that individual cone.

In contrast, in the mutant lines, the apparent cone threshold was displaced by ~1.5 log units to the right (~20 *R**/rod/20-ms flash) due to the absence of rod/cone gap junctions. Furthermore, cone

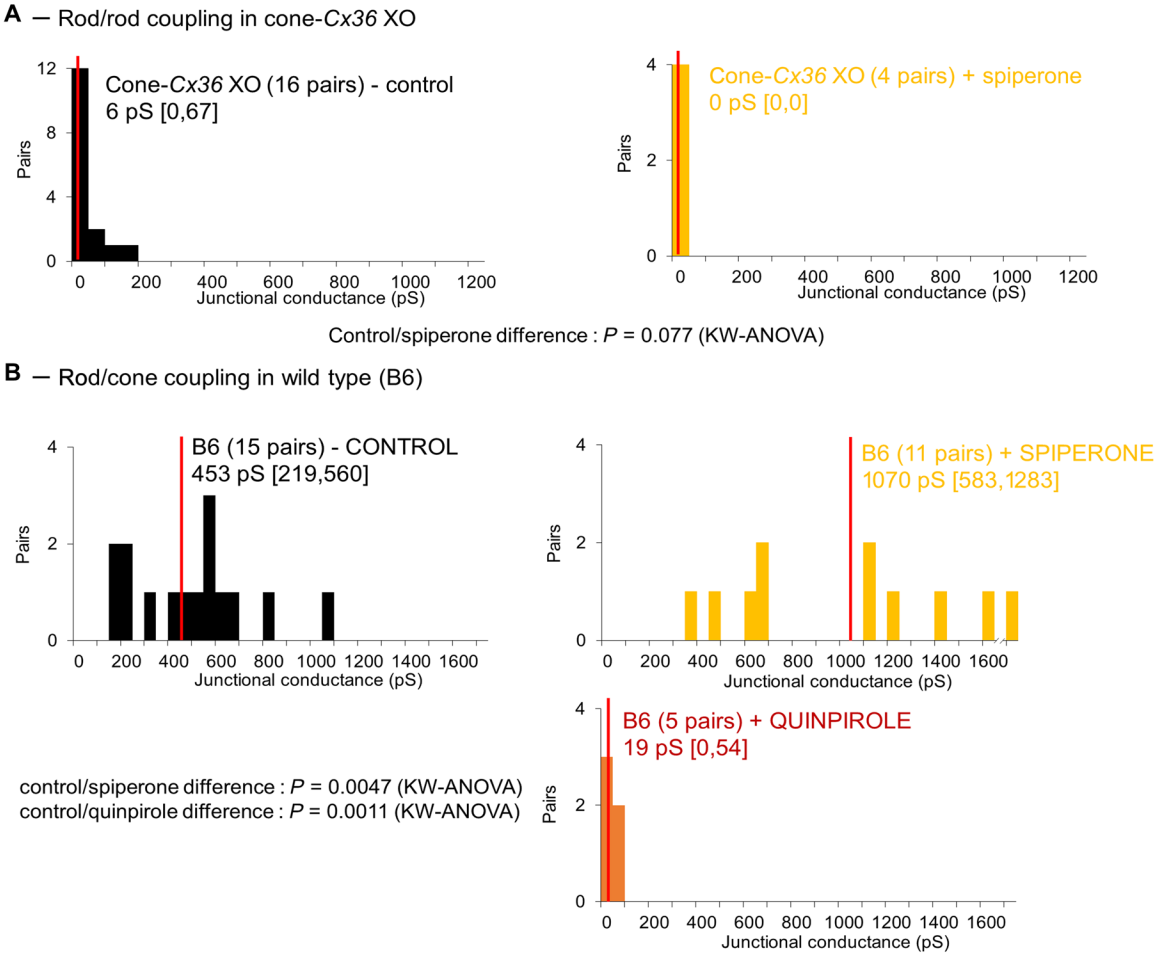

Fig. 4. The rod/cone gap junction is modulated by dopamine. (**A**) Effects of the D_2-like dopamine receptor antagonist spiperone on direct rod/rod coupling. Electrical coupling between pairs of adjacent rods was recorded in the cone-*Cx36* XO retina. No increase in coupling was observed when spiperone (10 μM) was present in the superfusion and applied for >10 min, indicating that spiperone has no effect on direct rod/rod coupling. (**B**) Effects of the D_2-like dopamine receptor antagonist spiperone and of the agonist quinpirole on rod/cone coupling. Electrical coupling between rod/cone pairs was recorded in wild-type (B6) retinas. Spiperone (10 μM; applied for >10 min, top) significantly increased rod/cone coupling, whereas quinpirole (1 μM; applied for >10 min, bottom) significantly decreased rod/cone coupling. Note the break of the *x* axis on the spiperone figure: The outlier value is 6040 pS. Numbers represent median value of the conductance [interquartile]. KW, Kruskal-Wallis.

responses were notably transient and lacked the characteristic rod after potential (Fig. 5A). The absence of rod signals in cones using the cone-specific *Cx36* XO speaks to the identity of the cone connexin, as expected. However, the same result in the rod-specific *Cx36* XO directly indicates that rods also express Cx36. The sensitivity of rod responses in both the rod- and cone-specific *Cx36* XOs was not significantly changed, which indicates that rods can function normally in the absence of rod/cone gap junctions (fig. S11). In addition, we did not find any significant differences in the resting membrane potential between the genotypes (table S1). In summary, the absence of rod-originating signals in cones in both rod-*Cx36* XO and cone-*Cx36* XO animals confirms that Cx36 is required for rod/cone coupling and reveals that Cx36 must be present on both sides of the junction for the transfer of rod signals to cones.

Modeling of photoreceptor coupling

To determine whether the values of rod conductance we measured are in agreement with indirect coupling through two consecutive rod/cone gap junctions, we used a computational model of the mouse photoreceptor network as previously developed using the trans-junctional conductances measured above (*20*). We modified the model to incorporate our new findings (e.g., no direct rod/rod coupling; see Material and Methods for details) (Fig. 6A). Because mouse photoreceptors have small terminals, coupling is restricted to the cone pedicle (within a sphere of ~10 μm of diameter), and rods are not directly coupled to other rods, we assumed a close to perfect space clamp of all terminals. Using a value of 300 pS for rod/cone coupling, we computed a value of rod coupling conductance of 81 pS. Assuming perfect space clamp also simplifies the arrangement to one in which three elements (rod, cone, and rod) are connected by two resistances (two rod/cone gap junctions, R1 and R2) placed in series. In this simplified case, the resulting resistance (between the two rods) can also be easily calculated from the formula $R_{total} = R1 + R2 = 2 \times$ rod/cone gap junction resistance. With conductance = 1/resistance and assuming that the gap junction resistance is much higher than the input resistance, we calculated that the strength of coupling between rods is 154 pS. Both estimates (81 and 154 pS) compare well with our measurements of rod coupling (128 pS;

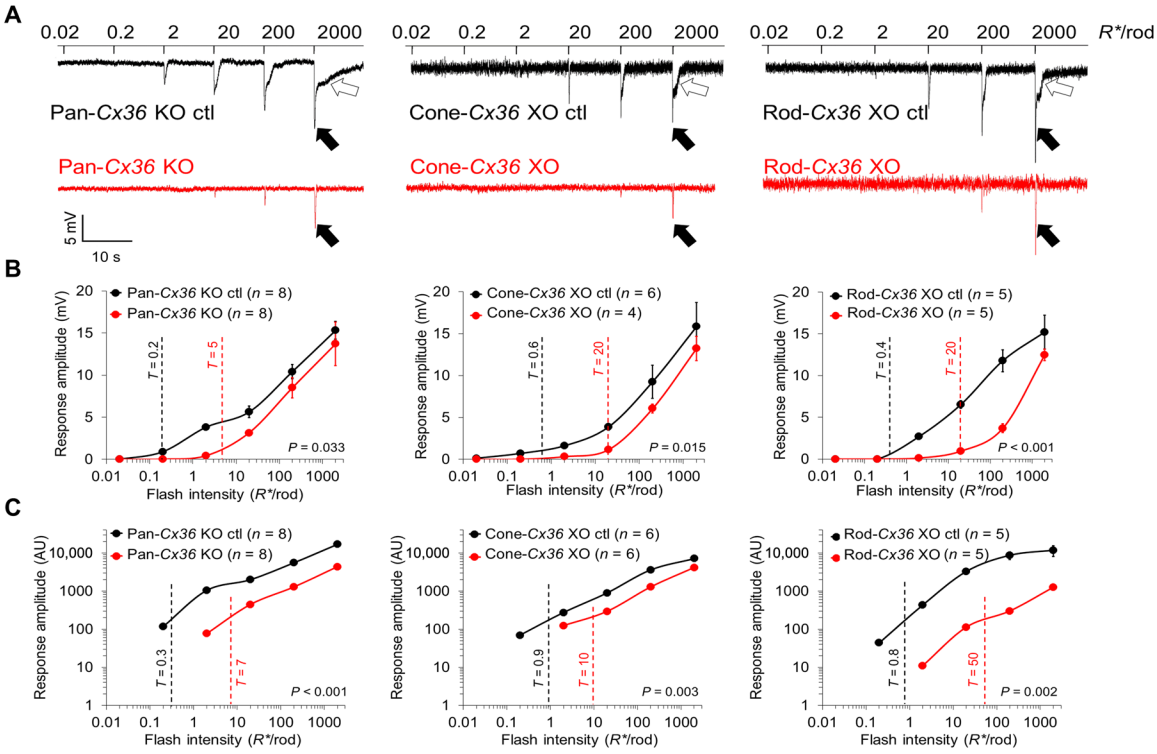

Fig. 5. The rod/cone gap junction is the entry of a major functional pathway. (**A**) Patch-clamp recordings of the light responses of cones obtained in wild-type and mutant retinas. Wild-type cone responses to brief flashes of light show two components: A fast and transient component (black arrow) and a slowly developing and recovering one (white arrow). Only the fast and transient component is present in mutant retinas, whereas the slow component is eliminated. We conclude that the fast component represents the cone intrinsic response and that the slow component represents the rod-mediated or cone extrinsic response via rod/cone gap junctions. (**B**) Average intensity-response curves of cones recorded under the conditions depicted in (A). Response is peak amplitude (in mV). Means ± SEM are shown. $n = 4$ to 8 cells per genotype. Threshold (T, vertical lines) is intensity to elicit a 1-mV response. (**C**) Average intensity-response curves of cones recorded under the conditions depicted in (A). Response is the area of the hyperpolarization [in arbitrary units (AU)]. Means ± SEM are shown. $n = 5$ to 8 cells per genotype. Threshold (T, vertical lines) shows intensity to elicit 200 AU.

fig. S10), supporting our interpretation that rods are indirectly coupled through cones.

Next, we tested the effects of rod/cone coupling on the spread of voltage between rods and cones (Fig. 6, B and C; see Material and Methods for details). Specifically, we tested whether varying the rod/cone junctional conductance recreated the recorded traces. Figure 6B shows that when rods and cones are decoupled (i.e., rod/cone coupling = 0 pS), the cone light responses have a high threshold (~20 R*/rod/flash) and transient kinetics. Increasing the rod/cone conductance up to (300 pS) decreased the threshold (~0.2 R*/rod/flash) and gradually increased the rod component, particularly at the brightest intensities. Intensity-response functions were computed for eight different values of rod/cone conductance, from 0 to 1 nS, and captured the dependence of the threshold and response amplitude on the junctional conductance (Fig. 6C). Thus, the model recapitulates the cone light responses. Last, modeling the rod light responses while varying the rod/cone gap junction conductance shows that coupling has little or no effect on rods (Fig. 6, D and E).

In summary, computer modeling of the photoreceptor network confirms our main findings: (i) Previously reported rod/rod coupling is indirect, and the rod/rod coupling conductance is consistent with the large size of the rod/cone conductance; (ii) at low light intensities, rods signals are faithfully transmitted to cones via gap junctions; and (iii) rods have a much greater influence on cones than cones have on rods, consistent with the anatomy we describe here, the high rod-to-cone convergence and the prevalence of rod/cone coupling.

DISCUSSION

Summary

Using rod- and cone-specific *Cx36* mutants and confocal imaging, we have identified all the photoreceptor gap junctions and shown that dopamine-modulated rod/cone coupling dominates the photoreceptor network. Because of their convergence, rod signals are transmitted to cone pedicles via rod/cone gap junctions at low light levels. Conversely, the effect of cones on rods is minimal because the cone signal must be divided among ~30 rods. This provides the functional advantage that rods can increase the sensitivity of cones without cones swamping the rods. Thus, primary and secondary rod pathways can coexist at the same level of light adaptation.

Rod/cone gap junctions are the most numerous in the OPL

Previous EM data have reported a variety of photoreceptor gap junctions in mammalian retina, including rod/rod, cone/cone, and rod/cone gap junctions (*4*, *6*, *8*, *9*). The confocal data presented here show that the gap junction protein Cx36 occurs where cone telodendria

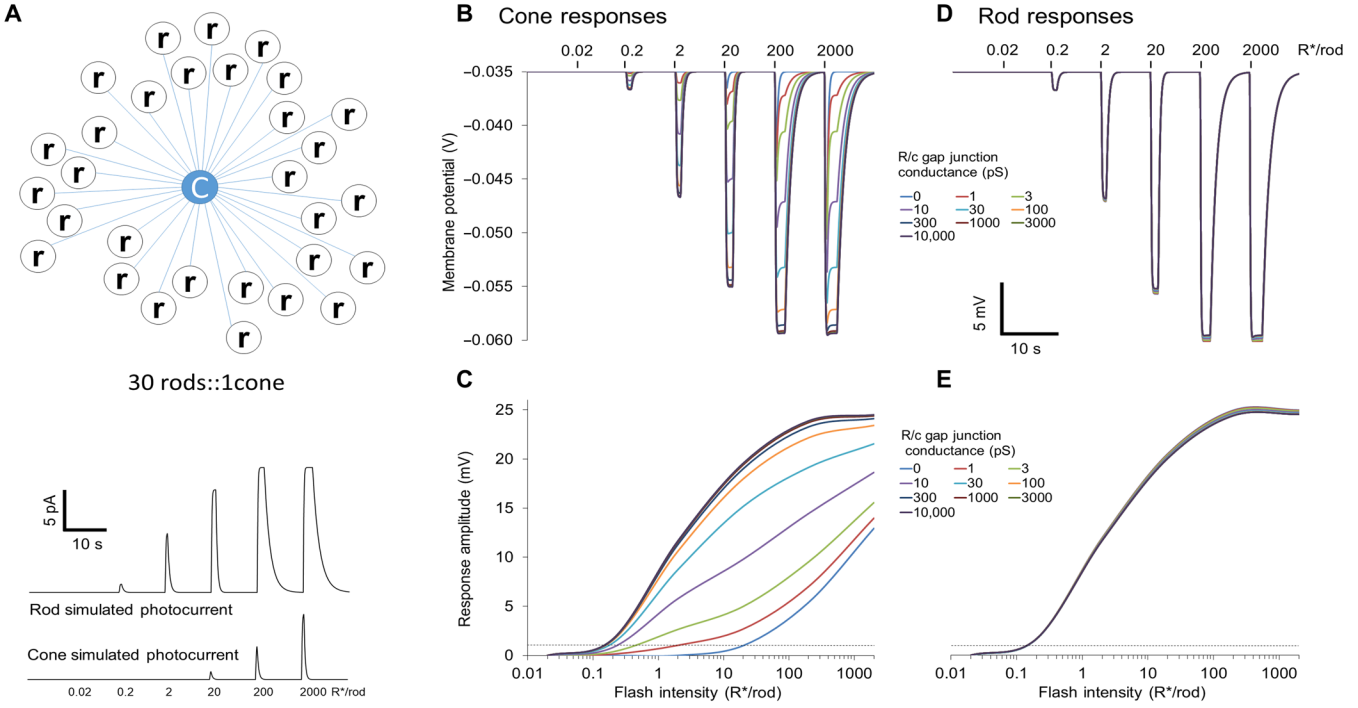

Fig. 6. Biophysical model of the photoreceptor network in mouse retina. (**A**) Model is based on a 30:1 rod/cone ratio. Simulated photocurrent functions are illustrated. (**B**) Cone voltage responses as a function of the rod/cone junctional conductance. The computational model recapitulates the wild-type cone light responses. (**C**) Intensity-response curves of cones computed for values of rod/cone junctional conductance ranging from 0 to 1000 pS. Note the decrease in threshold and increase in amplitude when the conductance increases. (**D**) Rod voltage responses as a function of the rod/cone junctional conductance and (**E**) intensity-response curves of rods computed for values of rod/cone junctional conductance ranging from 0 to 1000 pS. Note that rod/cone coupling has little effect on the response properties. (C and E) Dotted line shows criterion for threshold (1 mV).

contact every rod spherule close to the synaptic opening. These rod/cone gap junctions account for most of the photoreceptor coupling because they are eliminated in either the rod- or cone-specific *Cx36* XOs. We found no evidence for Cx36 at rod-to-rod contacts, and in the cone-*Cx36* XO, there was no remaining Cx36 labeling that we could attribute to rod/rod coupling. Thus, we were unable to identify the rod/rod gap junctions reported by Tsukamoto *et al.* (*8*). We could not identify cone/cone gap junctions in the wild-type mouse due to the large number of rod/cone gap junctions and the complexity of the telodendrial matrix. However, in the rod-*Cx36* XO, which should reveal cone coupling, we found a small number of potential cone/cone gap junctions. This is consistent with peripheral primate retina, where the density of the telodendrial matrix is low and the cone-to-cone contacts are much more prominent (*10*). These observations are consistent with our physiological and modeling data (see below) and suggest that rod/cone gap junctions account for most of photoreceptor coupling.

Cx36 is necessary and sufficient for the electrical coupling of mouse photoreceptors

In mammals, the presence of Cx36 in cones is well accepted (*15*, *16*), but inconsistent observations regarding Cx36 in mammalian rods have obscured its role in photoreceptor coupling. On the one hand, the presence of Cx36 in rods is supported by the expression of a *Cx36* gene expression reporter throughout the mouse ONL, in which rods represent ~97% of the cells (*39*). On the other hand, attempts to find *Cx36* mRNA expression in rods or Cx36 immunoreactivity on the rod side at rod/cone gap junctions or between rod spherules have led to negative (*12*, *14*) or inconclusive results (*10*, *11*, *40*). Recent electrophysiological data suggest that Cx36 is required for rod/cone coupling (*25*, *26*). However, using a pan-*Cx36* KO would be expected to block rod/cone coupling due to the elimination of cone *Cx36*, leaving open the possibility that rods express a different connexin or *Cx36* variant. Here, we demonstrate that Cx36 is required on both sides of the rod/cone gap junction for functional coupling. First, with confocal imaging, we located most Cx36 plaques at contacts between cone telodendria and the base of each rod spherule. Every rod spherule was coupled to one or more nearby cone pedicles. Assuming the gap junctions are homotypic, this implies Cx36 expression by both rods and cones. However, it leaves open the theoretical possibility that the gap junctions are heterotypic with cone Cx36 and a homolog on the rod side. Second, we found that Cx36 immunoreactivity at rod/cone contacts and electrical coupling between rods and cones were eliminated in animals that lack *Cx36* in either cones or rods. This indicates that Cx36 is required on both sides of the rod/cone gap junction. In other words, rod/cone gap junctions must be homotypic. Third, electrical coupling between rods is eliminated in the rod-*Cx36* XO, demonstrating that *Cx36* expression by rods is required for functional coupling between rods (even if it is indirect, see below). Last, transcriptomic analyses show that *Cx36* is expressed in both cones and rods and, importantly, that no other connexin is expressed in either cell type. Together, the data offer strong support that Cx36 is both necessary and sufficient for rod and cone electrical coupling, thereby solving

the long-standing discrepancy concerning the identity of the rod connexin in mammals.

Our results indicate that Cx36 is required and sufficient at both sides of the rod/cone gap junction. The absence of Cx36 on either side of the rod/cone gap junction reduces the conductance to zero (Fig. 3), which also indicates that there is no compensatory mechanism to the deletion of *Cx36*. In contrast, in other brain areas, such as the thalamic reticular nucleus (*41*, *42*) and the mesencephalic nucleus of the trigeminus (*43*), residual coupling was found in pan-*Cx36* KO mice. However, these studies could not conclude whether non-Cx36 junctions were present in addition or only as a compensatory response to *Cx36* deletion. Thus, Cx36-based coupling in distinct areas of the central nervous system either may include additional non-Cx36 gap junction channels or may have a compensatory mechanism to the deletion of *Cx36* that is lacking in photoreceptors.

Electrical coupling between rods is indirect via cones

While there is strong evidence for direct rod coupling in nonmammalian retina (*44*–*46*), we found that the organization of the mouse photoreceptor network is quite different. The rod/cone gap junction is its central element; cone/cone gap junctions are rare, and we could not detect rod/rod gap junctions. These unexpected results imply that electrical coupling between rods is not direct, but indirect, through intervening cones.

The following evidence supports this view. First, we found no anatomical support for direct rod coupling, a result that is mostly in agreement with histochemical studies from various mammalian species (*10*–*12*, *14*, *40*). Second, we found that electrical coupling between rods is abolished in cone-*Cx36* XO retinas, a mouse line that should reveal rod/rod coupling. This establishes that the rod/cone gap junction is essential for coupling between rods. In other words, rod coupling is indirect. Last, a simple computational model that excludes direct rod coupling and relies on rod/cone coupling recapitulates our measurements of rod coupling. Together, these lines of evidence support the view that the route of electrical coupling between rods is indirect via rod/cone gap junctions. Indirect or network coupling has been proposed as a route of apparent coupling in other neuronal systems, such as in the rat lateral vestibular nucleus (*3*, *47*). The demonstration of indirect rod electrical coupling via an intervening cone is analogous and supports this mechanism.

Our results may offer an explanation for previous unexpected findings. Previous studies that have suggested functional coupling between mammalian rods (*18*–*20*) also reported unusual tracer coupling patterns following the injection of single rods. Rods typically formed tracer pools of 1 to ~30 rods, but they were rarely organized in a continuous network, a pattern inconsistent with ideal coupling between direct neighbors. Yet, consistent with rod/cone coupling, these pools often contained faintly labeled cones. In light of our results, these tracer coupling patterns are more consistent with indirect coupling via cones rather than direct coupling between rods. Unless there are species differences between mammalian retinas, our study and others converge toward the view that rods in mammals are not directly coupled to their nearest neighbors. Instead, the incidence of rod/cone coupling is so prevalent that it may provide an indirect route for rod/cone/rod coupling.

Previous work has established that rod coupling is modulated by dopamine (*20*). If, in fact, indirect coupling is a consequence of rod/cone coupling, then this should also be controlled by dopamine. This is indeed the case, coupling between rod/cone pairs is almost shut down by a D_2-like agonist (quinpirole) and massively increased by the D_2-like antagonist spiperone, sometimes to a value >1000 pS (Fig. 4B). This indicates that indirect rod coupling is a proxy for rod/cone coupling and that circadian or light evoked dopamine release may control access to the secondary rod pathway.

Functional implications of rod/cone coupling

On the basis of the evidence presented here, rod/cone coupling is predominant in the OPL. Yet, this still provides an effective means of (indirect) rod coupling. Essentially, every rod is connected to a nearby cone, which is connected to all 30 rods in the immediate vicinity. Because each cone carries a signal equal to the mean of ~30 nearby rods, and because gap junctions are bidirectional, this means that rod signal is then shared with every individual rod. Previous studies have indeed demonstrated that rod signals can be shared within the network (*18*, *20*). Coupling also decreases uncorrelated random voltage noise present in individual rods (*48*). It has been proposed that for signals greater than ~1 isomerizations per rod per s (*R**/rod/s), rod coupling is beneficial because it increases the signal/noise ratio, helps circumvent saturation at the rod/rod bipolar cell synapse, and reduces trial-to-trial variability, thereby likely results in an optimization of rod signal processing (*18*–*20*).

However, the importance of rod coupling under dim light (scotopic) conditions remains uncertain. At these light levels, the signals in rods become rare and are essentially limited by Poisson fluctuations in photon absorption. Thus, for the photoreceptor network, synchronizing signals cannot be the main function of coupling.

The threshold of detectable light signals is approximately 1 photon per 10,000 rods/s due to the sensitivity of rods and convergence through the retinal circuitry. For a large part of the visual range, from the absolute visual threshold to more than 1 photon/rod/s, rod signaling is dependent on single-photon responses. In this range, rods act as single-photon detectors. However, the role of gap junctions is puzzling because it is clear that coupling will decrease the amplitude of the single-photon signal due to voltage spread through the network. For this specific reason, it was proposed that coupling must be low at night to preserve the single-photon amplitude and maximize the detection of scarce photons (*9*). However, the available evidence does not support this hypothesis. Photoreceptor coupling is high at night and low in the daylight hours due to the influence of light or circadian release of dopamine. In turn, the amplitude of single-photon responses is substantially reduced at night, primarily due to the dark-induced increase in photoreceptor coupling [from ~2.3 to ~1.1 mV (*20*)]. Thus, maintaining the single-photon amplitude at night may not be the highest priority. Instead, we suggest that concomitant noise reduction in the photoreceptor network, as reported by Jin *et al.* (*20*), is a major benefit from coupling. Previous studies have shown that the signal-to-noise ratio of threshold rod responses is only slightly reduced at night (*20*). Thus, we conclude that the benefit of noise reduction due to gap junction coupling may take precedence over maintaining the amplitude of the single-photon response.

MATERIALS AND METHODS

Animals

All animal procedures were reviewed and approved by the Animal Welfare Committee at the University of Texas Health Science Center at Houston or by our collaborators' local Institutional Animal Care and Use Committees. We used mice 2 to 6 months of age of either

sex. The $Cx36^{f/f}$ line was created and provided by D. Paul (Harvard University) who also provided the pan-$Cx36^{-/-}$ line. The $HRGP^{Cre}$ line was a gift from Y.-Z. Le (University of Oklahoma). The Rho^{i75Cre} line was developed by C.-K. Chen (Baylor college of Medicine) and provided by D. Krizaj (University of Utah). C57BL/6J (stock no. 000664) mice were purchased from the Jackson laboratories. The different mutant lines were backcrossed for more than five generations to the B6 background. Animals were housed under standard laboratory conditions, including a 12-hour light/12-hour dark cycle.

Generation of photoreceptor cell type–specific *Cx36* XO mouse lines

To generate photoreceptor cell type–specific Cx36 knockout lines, we mated mice from a line with a loxP-flanked allele of *Cx36* ($Cx36^{f/f}$) with mice of one of two lines that express the Cre recombinase in either the cones ($HRGP^{Cre}$) (*49*) or the rods (Rho^{i75Cre}) (*50*) (fig. S12). The $Cx36^{f/f}$ line has been described and validated in a recent paper, although retinal function was not tested in these animals (*51*). We found that mice of the $Cx36^{f/f}$ line have normal gross retinal function, as assessed by electroretinographic (ERG) recordings (fig. S13). Although the Rho^{i75Cre} and the $HRGP^{Cre}$ lines have been described before (*49*, *50*), we estimated the penetrance of Cre recombinase expression in these lines using the reporter *Ai9* (tdTomato). We found tdTomato protein expression in virtually all rods in Rho^{i75Cre};*Ai9* retinas (fig. S12A) and all cones, including blue cones, in $HRGP^{Cre}$;*Ai9* retinas (fig. S12, B to D), confirming the near-total penetrance of the Cre recombinase in these lines. Throughout the manuscript, we refer to Rho^{i75Cre};$Cx36^{f/f}$ as the rod-specific *Cx36* XO or rod-*Cx36* XO line and to $HRGP^{Cre}$;$Cx36^{f/f}$ as the cone-specific conditional *Cx36* knockout or cone-*Cx36* XO line. These conditional mouse lines are viable and fertile and do not show gross anatomical defects. We also used the constitutive (whole body) *Cx36* knockout line (*52*) and refer to it as the pan-*Cx36* KO line, and wild-type C56BL/6J mice referred to as B6 mice.

Histochemical detection of Cx36 in mouse retina

Antibodies and immunocytochemistry

Mice were anesthetized by intraperitoneal injection of a ketamine/xylazine mix solution (100/10 mg/kg) before being euthanized by cervical dislocation. Following the loss of cardiovascular function, the eyeballs were rapidly collected and placed in 4% paraformaldehyde in phosphate-buffered saline (PBS) at room temperature for 1 to 2 hours. Retinal cryosections or whole-mounted retinas were reacted with a cocktail of antibodies (Table 2) according to procedures described previously (*10*, *11*, *38*, *53*). Briefly, sections were blocked in 3% donkey serum/0.3% Triton X-100 (in PBS) for 2 hours (overnight for whole mounts) and incubated overnight at room temperature with primary antibody(ies) in 1% donkey serum/0.3% Triton X-100 (in PBS) (7 days for whole mounts). Following incubation with the primary antibody, sections were rinsed in PBS (6×, 20 min) and reacted with a secondary antibody(ies) for 2 hours (overnight for whole mounts) at room temperature in the dark. Donkey Alexa Fluor–, Cy3-, or DyLight-conjugated secondary antibodies were purchased from Jackson ImmunoResearch Laboratories Inc. (West Grove, PA) and used at 1:600 dilution. Last, sections or whole mounts were covered with mounting medium and sealed with nail polish. DAPI (4′,6-diamidino-2-phenylindole) (100 μg/ml) was added to the mounting medium to stain the nuclei.

Table 2. List of the primary antibodies used in this study.

Antibody	Immunogen	Source	Concentration
Connexin35/36 mouse monoclonal antibody, clone 8F6.2	Recombinant perch connexin35	Chemicon, catalog no. MAB3045	1:1000
Cone arrestin (cArr) rabbit polyclonal antibody	Synthetic peptide, C-terminal region of rat and mouse cArr	Millipore, catalog no. AB15282	1:500
Choline acetyl transferase (ChAT) goat polyclonal antibody	Human placenta enzyme	Chemicon, catalog no. AB144P	1:100
Vesicular glutamate transporter type I (VGLUT1) Guinea pig polyclonal antibody	Recombinant rat VGLUT1 (amino acids 456 to 500)	Synaptic Systems, catalog no. 135304	1:3000
Enhanced fluorescent green protein (eGFP) chicken polyclonal antibody	Recombinant GFP emulsified in Freund's adjuvant	Aves Labs Inc., catalog no. GFP-1010	1:100
S-cone opsin (blue cone opsin) rabbit polyclonal antibody	Recombinant human S-opsin	Millipore, catalog no. AB5407	1:400
Red fluorescence protein (RFP) rabbit polyclonal antibody	RFP fusion protein (full-length amino acid sequence) derived from the mushroom polyp coral *Discosoma*	Rockland antibodies and assays, catalog no. 600-401-379	1:500

Confocal microscopy

Images were digitally captured using either a LSM780 or a LSM800 Airyscan confocal microscope (Carl Zeiss Microscopy LLC, Thornwood, NY). Both systems operate with Zeiss' Zen software. The detector gain and offset parameters were adjusted so that the intensity of the most brightly labeled conditions showed very limited saturation. In addition, the settings were adjusted in the pan-*Cx36* KO retinas to pick up a little bit of background noise. This procedure ensured that the intensity of most pixels fell within the dynamic range of the detector. For each experiment, once settings were optimized, they remained unchanged for all genotypes to avoid imaging bias. Images were acquired using a 40× Plan-Apo 1.4 numerical aperture (NA) or a 63× Plan-Apo 1.4 NA objective (Zeiss) and additional digital magnification if needed. For sections, single or z-stacked images were taken within the region from 50 to 80% of the distance from

the optic nerve head to the periphery. For whole mounts, z-stacked images were acquired by placing the retina photoreceptors down and focusing through the inner retina. Images were exported as 16-bit TIFF files.

Quantification

The confocal images were analyzed with Fiji/ImageJ (imagej.nih.gov). To quantify Cx36 plaques in retinal sections, regions of interest (ROI) were selected. Ideally, one ROI included the entire thickness of a layer (e.g., OPL). The mean area (%) that the plaques represented and the mean intensity fluorescence signal were estimated for each ROI using the "Analyze particles" tool. Only one ROI count was used to represent one animal. Individual values were averaged from two to five animals.

Quantification of the number and volume of Cx36-positive puncta was performed on z-stacked images collected from whole-mounted retinas using Fiji/ImageJ and the "3D Objects Counter" tool. Z-stacks included 7 to 15 sections (45 by 45 by 0.4 μm), typically the OPL and most of the ONL. Cx36 plaques associated with bipolar cell dendrites were excluded from the analysis. Since the values of the plaque volume were not normally distributed, the median value was calculated for each animal to generate a single value in the OPL in one animal. The median values for three to six animals under each condition were then averaged. The detailed protocols of Cx36 quantification using Fiji are available upon request.

Immuno-EM

Two C57BL6 female 2-month-old mice were dark-adapted and enucleated. The anterior halves of the eyes were removed, and the posterior halves were fixed for 1 hour in 4% paraformaldehyde and 0.05% glutaraldehyde at room temperature and washed in PBS. The retinas were dissected free, treated with 1% sodium borohydride in PBS for 1 hour at room temperature, and washed in PBS overnight at 4°C. The retinas were flattened onto a membrane filter (MicronSep, 1215428) and washed further with PBS. The retinas were treated with an ascending and descending ethanol series (10, 25, 40, 25, 10% in PBS, 10 min each) and then embedded in 4% ultralow gelling temperature agarose (Sigma-Aldrich, A2576-25G) in PBS. The retinas were sectioned at 200 μm using a Leica VT 1000S vibratome. The sections were incubated in a mixture of monoclonal primary antibodies (see Table 2) in PBS with sodium azide at 4°C for 13 days. The sections were washed in PBS at room temperature at least three times for at least 30 min each, incubated in biotinylated donkey anti-mouse immunoglobulin G (Jackson ImmunoResearch Laboratories, catalog no. 715-066-150) in PBS at 4°C overnight, and then washed as before. The sections were incubated in ABC Vectastain (Vector Laboratories, PK4000 standard kit) overnight, washed, and then treated with 0.05% diaminobenzidine and 0.0025% hydrogen peroxide in PBS with 1.8% imidazole (Polyscience, 04008-5). The sections were washed and then treated with 1% osmium tetroxide in 0.1 M phosphate buffer (pH 7.4) for 1 hour. The sections were dehydrated at room temperature in methanol and embedded in Epon (PELCO Eponate 12, soft). The blocks were sectioned with a thickness of 0.1 to 0.2 μm, either vertically or tangentially, using a Leica EM UC7 ultramicrotome. The sections were collected onto 0.5 × 2–mm gold-coated single slot grids with formvar and carbon films (Electron Microscopy Sciences, FCF-205-Au). The sections were stained with 1% aqueous uranyl acetate for 15 min, sometimes followed by Reynolds lead citrate for 5 min. The images were acquired using a JEOL 2100 LaB6 electron microscope at 200 keV using a 100-μm condenser aperture and a 40-μm objective with a spot size of 2. For image collection, DigitalMicrograph was used to convert .dm3 files to .tif.

RNA-seq and analysis

Animals: Flow cytometry cell sorting

We used *Rho*^{i75Cre} and *HRGP*^{Cre} lines in which the Z/EG transgene was introduced. These animals express the CRE reporter enhanced green fluorescent protein (eGFP) in rods and cones, respectively. Retinas were isolated and enzymatically digested with trypsin (0.25%) for up to 15 min at 37°C. Subsequently, they were triturated with a plastic pipette tip in a deoxyribonuclease I solution (400 U/ml) to obtain single-cell suspension. During the whole procedure, the retinas were incubated in Hepes-buffered Ames' medium under room lights. Cell sorting was performed with an Aria II cell sorter (BD Biosciences). Selection was based on fluorescence and forward scatter. Collected cells were lysed and stored in the lysis buffer of a NucleoSpin RNA XS kit (Macherey-Nagel) until further treatment.

RNA-seq library preparation

GFP positive cells were sorted into TRIzol Reagent (Invitrogen) followed by RNA extraction according to the manufacturer's instructions. RNA quantity and quality were determined by Nanodrop 1000 (Thermo Fisher Scientific). RNA (100 ng) per sample was used for RNA-seq library preparation. Libraries were constructed using NEBNext Ultra Directional RNA Library Prep Kit for Illumina with NEBNext Poly(A) mRNA Magnetic Isolation Module (New England Biolabs) following the manufacturer's protocol. Libraries were quantified using Agilent 2100 Bioanalyzer (Agilent) and Quibit quantification. RNA-seq libraries were sequenced using NextSeq550 PE150 (Illumina).

RNA-seq and data analysis

We combined GENCODE M14 annotation file with NCBI (GCF_000001635.25_GRCm38.p5, only gene labeled as "lncRNA") (the official NCBI ftp repository: ftp://ftp.ncbi.nih.gov/genomes/refseq/vertebrate_mammalian/Mus_musculus/all_assembly_versions/GCF_000001635.25_GRCm38.p5/) as the final annotation file for mouse genome. Read mapping, transcript assembly, and expression estimation were performed as described in previous publication (*54*, *55*). The 150–base pair paired-end reads were aligned to the reference genome (mm10) using TopHat v2.1.0 with default parameters (*56*). FPKM (fragments per kilobase of transcript per million mapped reads) values for genes and transcripts annotated were analyzed by Cufflinks v2.2.1 (*57*). Any FPKM of <0.1 was set to 0.1 to avoid ratio inflation (*58*). Read counts for annotated genes and transcripts were obtained using HTSeq-count (*59*). Any FPKM differential expression genes (DEGs) were performed with DESeq2 (*60*). Genes with FPKM of >1 in at least one sample were retained for the analysis of DEGs. Genes were classified as DEGS: (i) At least one sample's FPKM of >1, (ii) $|\log_2(\text{fold change})| > 1$, and (iii) false discovery rate < 0.05.

In situ hybridization (RNAscope)

Eyeballs from wild-type (B6), pan-*Cx36* KO, cone-*Cx36* XO, and rod-*Cx36* XO animals were collected at P30 and dissected and fixed in fresh 10% neutral-buffered formalin for 24 hours. Samples were washed with PBS, dehydrated with serial ethanol, and embedded in paraffin. Sections were cut with a thickness of 9 μm. RNAscope ISH was performed using the RNAscope 2.5 HD Detection Reagents-BROWN kit following the manufacturer's protocol [Advanced Cell Diagnostics (ACD), catalog no. 322310]. According to ACD's instructions, each mRNA molecule hybridized to a probe appears as a separate brown color dot. The probes used were mouse *Gjd2* (catalog no. 506731).

Electrical recordings of photoreceptors

Photoreceptor coupling is expected to change according to light/dark adaptation and/or the action of circadian clocks (*16*). To minimize the influence of these confounding factors on our data, we used mice of B6 background, in which photoreceptor coupling has a weak/absent circadian component (*11*, *31*, *38*, *61*). We performed all the electrophysiology experiments during daytime and in darkness, when coupling is maximum. Before an experiment, animals were dark-adapted overnight.

Deep dark-adapted conditions were preserved during the entire duration of the tissue preparation using infrared light and night vision equipment. The procedure has been described in detail elsewhere (*31*, *32*). Briefly, mice were anesthetized and euthanized using ketamine/xylazine (100/10 mg/kg, i.p.) followed by cervical dislocation. One eye was enucleated and rapidly placed in Ames' medium with glutamine buffered with 23 mM $NaHCO_3$ (Sigma-Aldrich). The neural retina was isolated and placed on a filter paper (0.45-μm HAWP, Millipore). For pair recording of photoreceptors, retinal slices (250 μm) were cut with a razor blade tissue chopper (Stoelting) and rotated in the recording chamber to expose the retinal layers. Retinal tissue in the chamber was continuously perfused at 2 ml/min (turnover 1 /min) with bicarbonate-buffered Ames' solution at 32°C and continuously gassed with 5% CO_2/95% O_2 to maintain pH 7.4. Tissue was perfused for 60 min in the dark before the start of electrical recording. Full-field light stimulation was provided by a 175-W xenon arc lamp (Sutter Instruments). Calibrated neutral density filters and narrow-band interference filters were used to control light density and stimulus wavelength, respectively. Photoreceptors were stimulated with unpolarized monochromatic (500 nm, 10 nm half-width) light, and the duration of the stimulus was 20 ms. The intensity of the unattenuated stimulus at 500 nm was 2.18×10^{-4}W/cm^2 or 5.49×10^{14} photons/cm^2/s, converted to 2.06×10^6 isomerizations per rod per s (*R**/rod/s) (*20*).

Single or simultaneous paired recording of mouse photoreceptors. Patch clamp recordings of mouse photoreceptors were obtained as described previously (*20*, *31*, *32*). Briefly, electrodes were fashioned from borosilicate glass capillaries (outer diameter, 1.2 mm; inner diameter, 0.69 mm; Sutter Instruments). The pipette solution contained the following: 10 mM KCl, 120 mM K-D-gluconate, 5 mM MgCl2, 5 mM Na_2–adenosine 5′-triphosphate, and 1 mM Na_3–guanosine 5′-triphosphate. The pH was adjusted to 7.25 with KOH, and osmolarity was adjusted to 265 mOsm. Electrodes were backfilled with 25 μM β-escin (MP Biomedicals) with or without 0.5% Lucifer yellow (Sigma-Aldrich) in standard electrode solution. The tip resistance measured in the bath was 10 to 15 MΩ. The liquid junction potential (~15 mV) was not corrected. The preparation and electrode tips were visualized with infrared (>900 nm) differential interference contrast microscopy. For paired recordings, two independent micromanipulators (Sutter Instruments, MP285) were used to concomitantly position the two electrodes under visual control. Recordings were obtained with a 3900A amplifier (Dagan Corporation) and/or a 200B amplifier (Molecular Devices). We used positive pressure to give electrode tips clean access to photoreceptor membrane. The seal resistance ranged from 1 to 20 GΩ. Following perforation, which typically developed within 10 min, the series resistance was 15 to 30 MΩ. Signals were filtered at 1 kHz with a four-pole Bessel filter and sampled at 1 kHz.

To measure photoreceptor light responses, a single electrode recorded the membrane voltage under current clamp configuration (Io) while a series of 20-ms flashes of 500-nm light of increasing intensity was presented against a dark background. For paired recordings, both photoreceptors were held at −35 mV. Then, the voltage of one cell (slave) was held constant, and changes in membrane current were measured in response to voltage steps (50 ms, 10 mV increments from −50 to +50 mV) applied to the other cell (driver). A value of the transjunctional current was taken from the average of the values recorded between 20 and 30 ms after the beginning of the step. Statistical analysis of the light intensity response relationship was performed as previously described (*20*, *31*). Plots were generated from the average of the peak photovoltage amplitude (in mV) or of the entire area of the hyperpolarizing component of the response (in arbitrary units). As expected, transjunctional conductance recordings had a non-normal distribution, and we used nonparametric statistics to test for differences between groups, as previously described (*31*).

Electroretinographic recordings

Mice were dark-adapted overnight, and all procedures were performed under dim red light. Mice were anesthetized by intraperitoneal injection of a ketamine/xylazine mixture (90 and 9 mg/kg, respectively), and their pupils were dilated with a drop of 1% tropicamide. The anesthetized mice were then placed on a heating pad (37°C) inside a Ganzfeld ColorDome stimulator (Diagnosys, Espion E^2 system). Reference and ground electrodes were placed in the mouth and intradermally next to the tail, respectively. A drop of 2.5% hypromellose Gonak solution (Akorn) was applied to the eye, and gold loop electrodes were placed on the cornea under infrared illumination. After completing the setup procedure, mice were dark-adapted for 10 min before the start of recordings. Flash ERGs were elicited with single 4-ms green (500 nm) flashes ranging from (−3 to 5 log *R**/rod). The b-wave response amplitudes were measured as the difference in amplitude from the a-wave trough to the b-wave peak using Diagnosys software tools, and data were analyzed with SigmaPlot software (Systat Software Inc.).

Biophysical network model

We modified our previous model (*20*). The model was built in MATLAB R2018a (MathWorks Inc.) and based on 30 rods connected to 1 single cone. We set rod/rod conductance = 0 pS, cone/cone conductance = 0 pS, rod/cone conductance = 300 pS (default), rod input resistance = cone input resistance = 2.4 GΩ, and rod capacitance = rod capacitance = 5 pF, and we ignored voltage-gated conductances. Rod and cone current functions were modeled on the basis of actual recordings obtained in uncoupled cells; the purpose of the model was to test the influence of coupling and not the phototransduction or voltage-gated conductances. Gap junction conductance between rods and cones was modulated to recreate the rod and cone light responses.

Data analysis

Statistical analyses were performed with Clampfit 10.2 (Molecular Devices) and OriginPro 8.5.1 (OriginLab).

SUPPLEMENTARY MATERIALS

Supplementary material for this article is available at http://advances.sciencemag.org/cgi/content/full/6/28/eaba7232/DC1

View/request a protocol for this paper from *Bio-protocol*.

REFERENCES AND NOTES

1. J. E. Dowling, *The Retina: An Approachable Part of the Brain* (The Belknap Press of Harvard University, 2012).

2. A. L. Harris, Electrical coupling and its channels. *J. Gen. Physiol.* **150**, 1606–1639 (2018).
3. P. Alcamí, A. E. Pereda, Beyond plasticity: The dynamic impact of electrical synapses on neural circuits. *Nat. Rev. Neurosci.* **20**, 253–271 (2019).
4. E. Raviola, N. B. Gilula, Gap junctions between photoreceptor cells in the vertebrate retina. *Proc. Natl. Acad. Sci. U.S.A.* **70**, 1677–1681 (1973).
5. E. Raviola, N. B. Gilula, Intramembrane organization of specialized contacts in the outer plexiform layer of the retina. A freeze-fracture study in monkeys and rabbits. *J. Cell Biol.* **65**, 192–222 (1975).
6. H. Kolb, The organization of the outer plexiform layer in the retina of the cat: Electron microscopic observations. *J. Neurocytol.* **6**, 131–153 (1977).
7. Y. Tsukamoto, P. Masarachia, S. J. Schein, P. Sterling, Gap junctions between the pedicles of macaque foveal cones. *Vision Res.* **32**, 1809–1815 (1992).
8. Y. Tsukamoto, K. Morigiwa, M. Ueda, P. Sterling, Microcircuits for night vision in mouse retina. *J. Neurosci.* **21**, 8616–8623 (2001).
9. R. G. Smith, M. A. Freed, P. Sterling, Microcircuitry of the dark-adapted cat retina: Functional architecture of the rod-cone network. *J. Neurosci.* **6**, 3505–3517 (1986).
10. J. J. O'Brien, X. Chen, P. R. Macleish, J. O'Brien, S. C. Massey, Photoreceptor coupling mediated by connexin36 in the primate retina. *J. Neurosci.* **32**, 4675–4687 (2012).
11. H. Li, Z. Zhang, M. R. Blackburn, S. W. Wang, C. P. Ribelayga, J. O'Brien, Adenosine and dopamine receptors coregulate photoreceptor coupling via gap junction phosphorylation in mouse retina. *J. Neurosci.* **33**, 3135–3150 (2013).
12. E.-J. Lee, J.-W. Han, H.-J. Kim, I.-B. Kim, M.-Y. Lee, S.-J. Oh, J.-W. Chung, M.-H. Chun, The immunocytochemical localization of connexin 36 at rod and cone gap junctions in the guinea pig retina. *Eur. J. Neurosci.* **18**, 2925–2934 (2003).
13. A. Feigenspan, U. Janssen-Bienhold, S. Hormuzdi, H. Monyer, J. Degen, G. Söhl, K. Willecke, J. Ammermüller, R. Weiler, Expression of connexin36 in cone pedicles and OFF-cone bipolar cells of the mouse retina. *J. Neurosci.* **24**, 3325–3334 (2004).
14. P. Bolte, R. Herrling, B. Dorgau, K. Schultz, A. Feigenspan, R. Weiler, K. Dedek, U. Janssen-Bienhold, Expression and localization of connexins in the outer retina of the mouse. *J. Mol. Neurosci.* **58**, 178–192 (2016).
15. S. A. Bloomfield, B. Völgyi, The diverse functional roles and regulation of neuronal gap junctions in the retina. *Nat. Rev. Neurosci.* **10**, 495–506 (2009).
16. C. P. Ribelayga, J. O'Brien, Circadian and light-adaptive control of electrical synaptic plasticity in the vertebrate retina, in *Network Functions and Plasticity: Perspectives from Studying Electrical Coupling in Microcircuits*, J. Jing, Ed. (Elsevier, Cambridge, UK, 2017), pp. 209–241.
17. S. H. DeVries, X. Qi, R. G. Smith, W. Makous, P. Sterling, Electrical coupling between mammalian cones. *Curr. Biol.* **12**, 1900–1907 (2002).
18. E. P. Hornstein, J. Verweij, P. H. Li, J. L. Schnapf, Gap-junctional coupling and absolute sensitivity of photoreceptors in macaque retina. *J. Neurosci.* **25**, 11201–11209 (2005).
19. P. H. Li, J. Verweij, J. H. Long, J. L. Schnapf, Gap-junctional coupling of mammalian rod photoreceptors and its effect on visual detection. *J. Neurosci.* **32**, 3552–3562 (2012).
20. N. G. Jin, A. Z. Chuang, P. J. Masson, C. P. Ribelayga, Rod electrical coupling is controlled by a circadian clock and dopamine in mouse retina. *J. Physiol.* **593**, 1597–1631 (2015).
21. D. M. Schneeweis, J. L. Schnapf, Photovoltage of rods and cones in the macaque retina. *Science* **268**, 1053–1056 (1995).
22. D. M. Schneeweis, J. L. Schnapf, The photovoltage of macaque cone photoreceptors: Adaptation, noise, and kinetics. *J. Neurosci.* **19**, 1203–1216 (1999).
23. W. Li, S. Chen, S. H. DeVries, A fast rod photoreceptor signaling pathway in the mammalian retina. *Nat. Neurosci.* **13**, 414–416 (2010).
24. L. Cangiano, S. Asteriti, L. Cervetto, C. Gargini, The photovoltage of rods and cones in the dark-adapted mouse retina. *J. Physiol.* **590**, 3841–3855 (2012).
25. S. Asteriti, C. Gargini, L. Cangiano, Connexin 36 expression is required for electrical coupling between mouse rods and cones. *Vis. Neurosci.* **34**, E006 (2017).
26. N. T. Ingram, A. P. Sampath, G. L. Fain, Voltage-clamp recordings of light responses from wild-type and mutant mouse cone photoreceptors. *J. Gen. Physiol.* **151**, 1287–1299 (2019).
27. R. Nelson, Cones have rod input: A comparison of the response properties of cones and horizontal cell bodies in the retina of the cat. *J. Comp. Neurol.* **172**, 109–135 (1977).
28. C. Ribelayga, S. C. Mangel, Identification of a circadian clock-controlled neural pathway in the rabbit retina. *PLOS One* **5**, e11020 (2010).
29. G. D. Field, A. P. Sampath, F. Rieke, Retinal processing near absolute threshold: From behavior to mechanism. *Annu. Rev. Physiol.* **67**, 491–514 (2005).
30. S. A. Bloomfield, R. F. Dacheux, Rod vision: Pathways and processing in the mammalian retina. *Prog. Retin. Eye Res.* **20**, 351–384 (2001).
31. N. Jin, C. P. Ribelayga, Direct evidence for daily plasticity of electrical coupling between rod photoreceptors in the mammalian retina. *J. Neurosci.* **36**, 178–184 (2016).
32. N. Jin, Z. Zhang, K. A. Mankiewicz, C. P. Ribelayga, Paired recording to study electrical coupling between photoreceptors in mouse retina. *Methods Mol. Biol.* **2092**, 221–230 (2020).
33. Z. Kryger, L. Galli-Resta, G. H. Jacobs, B. E. Reese, The topography of rod and cone photoreceptors in the retina of the ground squirrel. *Vis. Neurosci.* **15**, 685–691 (1998).
34. P. K. Ahnelt, H. Kolb, The mammalian photoreceptor mosaic-adaptive design. *Prog. Retin. Eye Res.* **19**, 711–777 (2000).
35. C. J. Jeon, E. Strettoi, R. H. Masland, The major cell populations of the mouse retina. *J. Neurosci.* **18**, 8936–8946 (1998).
36. A. C. Miller, A. C. Whitebirch, A. N. Shah, K. C. Marsden, M. Granato, J. O'Brien, C. B. Moens, A genetic basis for molecular asymmetry at vertebrate electrical synapses. *eLife* **6**, e25364 (2017).
37. G. J. Hoge, K. G. V. Davidson, T. Yasumura, P. E. Castillo, J. E. Rash, A. E. Pereda, The extent and strength of electrical coupling between inferior olivary neurons is heterogeneous. *J. Neurophysiol.* **105**, 1089–1101 (2011).
38. Z. Zhang, H. Li, X. Liu, J. O'Brien, C. P. Ribelayga, Circadian clock control of connexin36 phosphorylation in retinal photoreceptors of the CBA/CaJ mouse strain. *Vis. Neurosci.* **32**, E009 (2015).
39. M. R. Deans, B. Volgyi, D. A. Goodenough, S. A. Bloomfield, D. L. Paul, Connexin36 is essential for transmission of rod-mediated visual signals in the mammalian retina. *Neuron* **36**, 703–712 (2002).
40. L. Dang, S. Pulukuri, A. J. Mears, A. Swaroop, B. E. Resse, A. Sitaramayya, Connexin 36 in photoreceptor cells: Studies on transgenic rod-less and cone-less mouse retinas. *Mol. Vis.* **10**, 323–327 (2004).
41. S.-C. Lee, S. L. Patrick, K. A. Richardson, B. W. Connors, Two functionally distinct networks of gap junction-coupled inhibitory neurons in the thalamic reticular nucleus. *J. Neurosci.* **34**, 13170–13182 (2014).
42. T. A. Zolnik, B. W. Connors, Electrical synapses and the development of inhibitory circuits in the thalamus. *J. Physiol.* **594**, 2579–2592 (2016).
43. S. Curti, G. Hoge, J. I. Nagy, A. E. Pereda, Synergy between electrical coupling and membrane properties promotes strong synchronization of neurons of the mesencephalic trigeminal nucleus. *J. Neurosci.* **32**, 4341–4359 (2012).
44. J. Zhang, S. M. Wu, Connexin35/36 gap junction proteins are expressed in photoreceptors of the tiger salamander retina. *J. Comp. Neurol.* **470**, 1–12 (2004).
45. J. Zhang, S. M. Wu, Physiological properties of rod photoreceptor electrical coupling in the tiger salamander retina. *J. Physiol.* **564**, 849–862 (2005).
46. D. Attwell, M. Wilson, S. M. Wu, A quantitative analysis of interactions between photoreceptors in the salamander (Ambystoma) retina. *J. Physiol.* **352**, 703–737 (1984).
47. H. Korn, C. Sotelo, F. Crepel, Electrotonic coupling between neurons in the rat lateral vestibular nucleus. *Exp. Brain Res.* **16**, 255–275 (1973).
48. T. D. Lamb, E. J. Simon, The relation between intercellular coupling and electrical noise in turtle photoreceptors. *J. Physiol.* **263**, 257–286 (1976).
49. Y.-Z. Le, J. D. Ash, M. R. Al-Ubaidi, Y. Chen, J.-X. Ma, R. E. Anderson, Targeted expression of Cre recombinase to cone photoreceptors in transgenic mice. *Mol. Vis.* **10**, 1011–1018 (2004).
50. S. Li, D. Chen, Y. Sauvé, J. McCandless, Y.-J. Chen, C.-K. Chen, Rhodopsin-iCre transgenic mouse line for Cre-mediated rod-specific gene targeting. *Genesis* **41**, 73–80 (2005).
51. X. Yao, J. Cafaro, A. J. McLaughlin, F. R. Postma, D. L. Paul, G. Awatramani, G. D. Field, Gap junctions contribute to differential light adaptation across direction-selective retinal ganglion cells. *Neuron* **100**, 216–228.e6 (2018).
52. M. R. Deans, J. R. Gibson, C. Sellitto, B. W. Connors, D. L. Paul, Synchronous activity of inhibitory networks in neocortex requires electrical synapses containing connexin36. *Neuron* **31**, 477–485 (2001).
53. X. Liu, Z. Zhang, C. P. Ribelayga, Heterogeneous expression of the core circadian clock proteins among neuronal cell types in mouse retina. *PLOS One* **7**, e50602 (2012).
54. R. C.-D. Duran, H. Yan, Y. Zheng, X. Huang, R. Grill, D. H. Kim, Q. Cao, J. Q. Wu, The systematic analysis of coding and long non-coding RNAs in the sub-chronic and chronic stages of spinal cord injury. *Sci. Rep.* **7**, 41008 (2017).
55. Y. Zhang, K. Chen, S. A. Sloan, M. L. Bennett, A. R. Scholze, S. O'Keeffe, H. P. Phatnani, P. Guarnieri, C. Caneda, N. Ruderisch, S. Deng, S. A. Liddelow, C. Zhang, R. Daneman, T. Maniatis, B. A. Barres, J. Q. Wu, An RNA-sequencing transcriptome and splicing database of glia, neurons, and vascular cells of the cerebral cortex. *J. Neurosci.* **34**, 11929–11947 (2014).
56. C. Trapnell, L. Pachter, S. L. Salzberg, TopHat: Discovering splice junctions with RNA-seq. *Bioinformatics* **25**, 1105–1111 (2009).
57. C. Trapnell, A. Roberts, L. Goff, G. Pertea, D. Kim, D. R. Kelley, H. Pimentel, S. L. Salzberg, J. L. Rinn, L. Pachter, Differential gene and transcript expression analysis of RNA-seq experiments with TopHat and cufflinks. *Nat. Protoc.* **7**, 562–578 (2012).
58. J. Quackenbush, Microarray data normalization and transformation. *Nat. Genet.* **32**, 496–501 (2002).
59. S. Anders, P. T. Pyl, W. Huber, HTSeq–A python framework to work with high-throughput sequencing data. *Bioinformatics* **31**, 166–169 (2015).
60. M. I. Love, W. Huber, S. Anders, Moderated estimation of fold change and dispersion for RNA-seq data with DESeq2. *Genome Biol.* **15**, 550 (2014).
61. Z. Zhang, E. Silveyra, N. Jin, C. P. Ribelayga, A congenic line of the C57BL/6J mouse strain that is proficient in melatonin synthesis. *J. Pineal Res.* **65**, e12509 (2018).

Acknowledgments: We thank E. Silveyra (UT Houston), S. Raman (Rice University), E. Baseri (University of Houston), P. J. Masson (University of Houston), A. Z. Chuang (UT Houston), M. B. Sherman (UT Medical Branch in Galveston), and W. S. Liu (UT Houston) for the help with some of the initial experiments. We thank C. M. Craft (USC) for donating antibodies in the early stages of this project. **Funding:** This work was supported by grants from the NIH grant numbers R01-NS088353 (to J.W.), R21-EY028647 (to C.P.R. and J.W.), R01-EY029408 (to C.P.R. and S.C.M.), R01-EY024376 (to C.-A.M), P30-EY028102 (to S.C.M.), a UTHealth BRAIN Initiative/CTSA grant TR000371 (to C.P.R. and J.W.), a grant from the University of Texas System Neuroscience and Neurotechnology Research Institute no. 362469 (to C.P.R. and J.W.), the Staman Ogilvie Fund-Memorial Hermann Foundation (to J.W.), and the Herman Eye Fund (Ruiz Department of Ophthalmology and Visual Science). **Author contributions:** C.P.R. and S.C.M. designed the study, performed the analyses, and wrote the manuscript with input from all other authors. F.P. and D.L.P. developed the *Cx36*$^{f/f}$ mouse line. Z.Z. created the photoreceptor cell type–specific *Cx36* conditional knockout mouse lines. N.J., I.F., and L.-M.T. performed the electrophysiology experiments. M.I., J.K., S.C.M., C.P.R., and S.B.Y. performed the immunofluorescence detection of Cx36 in the retina, acquired confocal images, and performed quantifications. D.W.M. performed the immuno-EM experiments. C.P.R. and I.F. developed the mathematical model of the photoreceptor network. E.S. and Y.U. did the ERG recordings. C.-A.M. and T. K. designed and performed the RNAscope experiments. Z.Z., Y.Y., H.W., and J.W. performed the RNA-seq and analysis experiments. **Competing interests:** The authors declare that they have no competing interests. **Data and materials availability:** All data needed to evaluate the conclusions in the paper are present in the paper and/or the Supplementary Materials. Additional data or protocols related to this paper may be requested from the authors. The pan-*Cx36* KO, rod-*Cx36* XO, and cone-*Cx36* XO lines can be provided by C.P.R. or S.C.M. pending scientific review and a completed material transfer agreement.

Submitted 28 December 2019
Accepted 21 April 2020
Published 8 July 2020
10.1126/sciadv.aba7232

Citation: N. Jin, Z. Zhang, J. Keung, S. B. Youn, M. Ishibashi, L.-M. Tian, D. W. Marshak, E. Solessio, Y. Umino, I. Fahrenfort, T. Kiyama, C.-A. Mao, Y. You, H. Wei, J. Wu, F. Postma, D. L. Paul, S. C. Massey, C. P. Ribelayga, Molecular and functional architecture of the mouse photoreceptor network. *Sci. Adv.* **6**, eaba7232 (2020).